Comparison of Numerical Solvers for Cavitating Flows

Eric Goncalvès da Silva, Maxime Champagnac, Regiane . Fortes Patella

International Journal of Computational Fluid Dynamics
Vol. 00, No. 00, February 2010, 1–43

RESEARCH ARTICLE

Comparison of Numerical Solvers for Cavitating Flows

E. Goncalves [a]*, M. Champagnac [a] and R. Fortes Patella[a]

[a] *LEGI, Grenoble-INP, 1025 rue de la Piscine, 38400 St Martin d'Heres, France*

(*Received 00 Month 200x; final version received 00 Month 200x*)

Different computational fluid dynamics (CFD) strategies have been developed to simulate, analyze and better understand cavitating flows. Based on homogeneous models, two numerical approaches using compressible and incompressible codes, are applied to capture large density variations and unsteady behaviours of cavitating flows. Simulations are performed on two-dimensional Venturi geometries and compared with experimental data. Local and global analyses are proposed and the necessity to account for compressibility phenomena is discussed.

Keywords: Two-phase flow ; cavitation ; homogeneous models ; numerical schemes

Nomenclature

c	speed of sound
C_P, C_V	thermal capacities
E	total energy
e	internal energy
F_c, F_d	convective and diffusive flux densities
H	total enthalpy
h	enthalpy
k	turbulent kinetic energy
M	local Mach number
M_∞	infinite Mach number
n	outer normal to a surface
P	static pressure
P_i	stagnation temperature
P_{vap}	vapour pressure
P_r, P_{rt}	Prandtl numbers
P_∞	reference pressure
q	total heat flux
q_{ref}	energy of fluid at a given reference state
Re_L	Reynolds number based on the length L
T	mean static temperature
T_i	stagnation temperature
T_{ref}	reference temperature
W	conservative variables

*Corresponding author. Email: eric.goncalves@legi.grenoble-inp.fr

ISSN: 1029-8436 print/ISSN 1477-268X online

DOI: 10.1080/1029843YYxxxxxxxx
http://www.informaworld.com

α	void ratio
β	parameter of the preconditioning method
γ	ratio of thermal capacities
$\lambda_{\pm}$	eigenvalues of the preconditioned inviscid system
$\delta(.)_{l+1/2}$	difference operator for the l direction: $(.)_{l+1} - (.)_l$
$\mu(.)_{l+1/2}$	averaged operator for the l direction: $((.)_{l+1} + (.)_l)/2$
ε	dissipation rate
μ, μ_t	molecular and eddy viscosity
ρ	density
$\rho(A)$	spectral radius of matrix A
ρ^V	viscous spectral radius
σ	cavitation number
$\overline{\overline{\tau}}$	total stress tensor
Ω	cell volume
$()_L$	liquid value
$()_V$	vapour value
$()^n$	value at temporal iteration n

1 INTRODUCTION

The capability for simulation and prediction of cavitating flows is of critical importance in the design of equipment such as turbomachinery, turbopumps in rocket propulsion systems, hydrofoils, fuel injectors, marine propellers, nozzles and underwater bodies. In most cases, cavitation is an undesirable phenomenon, causing significant degradation in the performance: reduced flow rates, lower pressure increases in pumps, load asymmetry, vibrations, noise and erosion. In most industrial applications, cavitating flows are turbulent and the dynamics of the formed interface involves complex interactions between vapour and liquid phases. These interactions are not well understood in the closure region of cavities where a distinct interface may not exist and where the flow is unsteady.

A number of physical and numerical models have been developed to investigate cavitating flows. Two-phase flow is often treated as a homogeneous phase mixture. A homogeneous mixture consists of a single fluid of varying density ρ. In the mixture, the phases are assumed to be in kinematic, mechanical and thermal equilibrium: they share the same velocity, pressure and temperature. Moreover, vaporization or condensation processes are assumed to be instantaneous. Hence, this approach cannot reproduce strong thermodynamic or kinetic non-equilibrium effects. Density variation is determined by a cavitation model. In the literature, cavitation modelling is often based on either "equation of state (EOS)" models or "void ratio transport equation" models. In the EOS method, to close the system, the density is related to the pressure and the temperature (Delannoy and Kueny 1990, Song 2002, Liu *et al.* 2004, Moreau *et al.* 2004, Sinibaldi *et al.* 2006, Pouffary *et al.* 2008, Goncalves and Fortes-Patella 2009). In the second approach, the system is closed by adding a transport equation for the void ratio including a cavitation source term (Kunz *et al.* 2000, Ahuja *et al.* 2001, Senocak and Shyy 2002, Singhal *et al.* 2002, Wu *et al.* 2005, Fortes-Patella *et al.* 2006).

The crucial requirement of multiphase codes is the ability to accurately and efficiently span both incompressible and compressible flow regimes. Cavitating flows are characterized by large variation of the local Mach number. Indeed the speed of sound can be several orders of magnitude higher in the liquid phase than in the two-phase mixture (supersonic regime). Thus for low speed applications, numerical methods must be able to properly simulate simultaneously

nearly-incompressible and highly-compressible flow areas. In the literature, both incompressible and compressible solvers have been used. The first category must include density variations for cavitating applications; for example with SIMPLE or PISO pressure-based algorithms (Ventikos and Tzabiras 2000, Senocak and Shyy 2002, Singhal *et al.* 2002, Coutier-Delgosha *et al.* 2003, Wu *et al.* 2005, Fortes-Patella *et al.* 2006). On the other hand, compressible codes require an appropriate equation of state to cover all possible fluid states (pure liquid, two-phase mixture and pure vapour). A well known difficulty concerns the stiffness on the solution convergence when the Mach number becomes low. In this situation, the dominance of convection terms renders the system stiff and compressible solvers converge slowly. To overcome this difficulty, a preconditioned method is necessary. The physical acoustic waves are replaced by pseudo-acoustic modes much closer to the advective velocity, reducing stiffness and enhancing the convergence. A number of studies have been carried out with different preconditioned compressible solvers (Edwards and Franklin 2000, Kunz *et al.* 2000, Ahuja *et al.* 2001, Schmidt *et al.* 2006, Sinibaldi *et al.* 2006, Goncalves and Fortes-Patella 2009). Both approaches seem to have strong and weak points. According to (Ahuja *et al.* 2001), incompressible codes can lead to an erroneous acoustic speed in the mixture, particularly in the interface region, which may be not appropriate for unsteady simulations. Both CFD algorithms have been compared in (Venkateswaran *et al.* 2002) and applied to unsteady cavitating ogive flows. Computational results showed distinct behaviours between codes regarding the re-entrant jet phenomenon: with the incompressible code, the phenomenon was more developed and reached the leading edge of the cavity. The authors concluded that compressibility effects may need to be taken into account to correctly describe the cavity dynamics. Finally, a third method combining the advantages of the first two approaches has been explored (Rossow 2007, Housman 2009) and provided interesting results.

In the present study, we present two in-house finite-volume codes solving the one-fluid RANS equations with an EOS cavitation model. In the mixture, a barotropic EOS is used to close the system for both codes. Two numerical approaches have been tested. The first code is an incompressible pressure-based solver modified to consider density variations. Both pure phases are assumed incompressible. The second approach is based on a compressible density-based code with a preconditioning method. Both pure phases are compressible and follow the stiffened gas EOS.

The models and numerical techniques are evaluated by comparing the numerical results with experimental data on two Venturi geometries with cold water (Fortes-Patella *et al.* 2006, Barre *et al.* 2009). In the following, we will first summarize the essential elements of the governing equations, modelling concepts and numerical schemes before presenting the computational results.

2 EQUATION OF STATE: THE BAROTROPIC LAW

The cavitation model applied in the present work is based on a sinusoidal barotropic law (Delannoy and Kueny 1990) (Figure 1). This law is characterized by an adjustable parameter c_{min} which can be interpreted as the minimum speed of sound in the mixture. This parameter is set to 0.86 m/s for both codes.

When the pressure is between $P_{vap} + \Delta P$ and $P_{vap} - \Delta P$, the following relationship applies, function of the void ratio α:

$$P(\alpha) = P_{vap} + \left(\frac{\rho_L^{sat} - \rho_V^{sat}}{2} \right) c_{min}^2 \, \mathrm{Arcsin}\,(1 - 2\alpha) \quad \text{and} \quad \alpha = \frac{\rho - \rho_L^{sat}}{\rho_V^{sat} - \rho_L^{sat}} \tag{1}$$

where ΔP represents the pressure width of the law, ρ_L^{sat} and ρ_V^{sat} are the saturation values of

liquid and vapour densities. For a void ratio value of 0.5, the pressure is equal to the saturation pressure P_{vap}.

For cold water, the cavitation phenomenon is assumed to be isothermal. The speed of sound can be easily computed :

$$c^2 = \left(\frac{\partial P}{\partial \rho}\right)_s = \left(\frac{\partial P}{\partial \rho}\right)_T = \frac{c_{min}^2}{\sqrt{1-(1-2\alpha)^2}} \tag{2}$$

This speed is always strictly positive and thus the inviscid compressible system is hyperbolic. Moreover, this mixture EOS is convex for the c_{min} value considered (i.e. the Hessian matrix of internal energy has to be positive definite) and respects entropy conditions (Goncalves and Fortes-Patella 2009).

3 THE INCOMPRESSIBLE SOLVER

The IZ code, supported by the French space agency CNES, is based on an incompressible approach adapted to two-dimensional cavitating flows. The numerical resolution is a pressure-correction method derived from the SIMPLE algorithm. It uses a finite-volume discretization applied to structured orthogonal meshes with staggered grids. All computations are time-dependent to take into account the variation of density. Other applications are presented in (Coutier-Delgosha *et al.* 2002, 2003, Fortes-Patella *et al.* 2006).

3.1 *Governing equations*

The RANS equations coupled with a two-equation $k-\varepsilon$ turbulence model are solved in the orthogonal frame of curvilinear coordinates (ξ,η). The system can be expressed as :

$$\frac{\partial W}{\partial t} + \frac{1}{J}\frac{\partial}{\partial \xi}\left[h_2\left(uW - \frac{F_W}{h_1}\frac{\partial (W/\rho)}{\partial \xi}\right)\right] + \frac{1}{J}\frac{\partial}{\partial \eta}\left[h_1\left(vW - \frac{F_W}{h_2}\frac{\partial (W/\rho)}{\partial \eta}\right)\right] = S_W \tag{3}$$

$$W = \begin{pmatrix} \rho \\ \rho u \\ \rho v \\ \rho k \\ \rho \varepsilon \end{pmatrix} \quad F_W = \begin{pmatrix} 0 \\ \mu + \mu_t \\ \mu + \mu_t \\ \mu_t/\sigma_k \\ \mu_t/\sigma_\varepsilon \end{pmatrix} \quad S_W = \begin{pmatrix} 0 \\ \frac{-1}{J}\frac{\partial (h_2 P)}{\partial \xi} \\ \frac{-1}{J}\frac{\partial (h_1 P)}{\partial \eta} \\ \mu_t\left(\left[\frac{1}{J}\frac{\partial (h_2 v)}{\partial \xi}\right]^2 + \left[\frac{1}{J}\frac{\partial (h_1 u)}{\partial \eta}\right]^2\right)\rho\varepsilon \\ C_1 k\left(\left[\frac{1}{J}\frac{\partial (h_2 v)}{\partial \xi}\right]^2 + \left[\frac{1}{J}\frac{\partial (h_1 u)}{\partial \eta}\right]^2\right) - S_\varepsilon \end{pmatrix}$$

where W denotes the conservative variables, h_1 and h_2 the scale factors (the square roots of the diagonal components of the metric tensor) and $J = h_1 \times h_2$, u and v the velocity components along coordinates ξ and η respectively. The quantities σ_k, σ_ε, C_1 and S_ε depend on the formulation of the turbulence model.

3.2 *Spatial discretization*

The finite volume method is applied for the space discretization. Each equation is integrated locally on its own control volume based on the staggered grid to avoid pressure oscillations.
The pressure and the density are calculated at the center of the cells, while the velocity components u and v are located respectively on the western and the southern faces of each cell.
The diffusive terms are discretized with a second-order space-centered scheme, while the convection terms are estimated through the second-order HLPA (Hybrid Linear Parabolic Approximation) scheme (Zhu 1991). This is a second-order scheme, which locally switches to first order, to prevent numerical oscillations in critical high pressure or high density gradient areas.

3.3 *Temporal discretization*

Several first and second order numerical schemes are available. An unconditionally stable second-order implicit scheme is applied to compute values at iteration $n+1$:

$$\frac{\partial W}{\partial t} = \frac{3W^{n+1} - 4W^n + W^{n-1}}{2\Delta t} \tag{4}$$

3.4 *Turbulence model*

A $k-\varepsilon$ RNG turbulent closure model (Yakhot *et al.* 1992), modified for two-phase flow simulations by adding a turbulent viscosity limiting function $f(\rho)$, is used. The turbulent viscosity satisfies:

$$\mu_t = f(\rho) C_\mu \frac{k^2}{\varepsilon} \quad \text{where} \quad C_\mu = 0.085 \tag{5}$$

In pure phases, $f(\rho) = \rho$. In the two-phase mixture regions, an arbitrary decrease of the turbulent viscosity was proposed by Reboud (Reboud *et al.* 1998, Coutier-Delgosha *et al.* 2002):

$$f(\rho) = \rho_V + (1-\alpha)^n (\rho_L - \rho_V) \tag{6}$$

where n is a parameter greater than 1. In the present study, we have chosen the value $n = 10$. The turbulence model is coupled with standard wall functions.

3.5 *Iterative procedure*

If the flow is incompressible, we use a classical pressure-correction method proposed by Patankar (Patankar and Spalding 1972). It is based on the SIMPLE algorithm, modified to include the cavitation treatment. The resolution of each time-step is divided into several iterations, until convergence is reached. Each iteration is composed of successive steps. The velocities are first estimated from the momentum equations with a pressure field. Then, values of velocities are corrected by solving a Poisson pressure correction equation in order to satisfy continuity. The cavitation process induces the following modifications:

- The density is first calculated with the barotropic state law after solving the momentum equations, as well as its derivative $\dfrac{\partial \rho}{\partial P}$.
- When the pressure correction dP is obtained, the density values are corrected using the relation: $d\rho = \left(\dfrac{\partial \rho}{\partial P}\right) dP$

The main steps of a single iteration are listed next to determine values at iteration $n+1$:

a) Resolution of the transport equations for the turbulent variables and calculation of the turbulent viscosity.
b) Calculation of the estimated velocities U^* from the momentum balance equations.
c) Calculation of the intermediate density ρ^* and its derivative with respect to the pressure, according to the equation of state.
d) Resolution of the pressure correction equation, which involves not only velocity variations dU but also supplementary density variations terms $d\rho$.
e) Computation of the new velocity U^{n+1}, pressure P^{n+1} and density ρ^{n+1} fields.

A loop is added to the pressure correction step inside each iteration to check that the void ratio remains between 0 and 1. Moreover, the density, velocity components and turbulent variables can be under-relaxed if convergence is difficult to obtain. The pressure correction is not relaxed.

3.6 *Inlet and outlet conditions*

The boundary conditions are based on a system of dummy cells. Classical incompressible types of boundary conditions are applied:
- at the inlet, the velocity component u is imposed and the component v is set to 0.
- at the outlet, a static pressure is imposed, and if the velocity component $u < 0$, the gradient $\dfrac{\partial v}{\partial x}$ is set to 0.
We assume that inlet and outlet areas are in a pure liquid region. No cavitation appears in these boundaries.

4 THE COMPRESSIBLE SOLVER

The CaviFlow code solves the compressible one-fluid RANS system for multi-domain structured meshes. It is based on a cell-centered finite-volume discretization. More details concerning the code are given in (Goncalves and Fortes-Patella 2009).

4.1 *Preconditioning method for the Euler system*

The preconditioning method is based on the modification of the derivative term by a pre-multiplication with a suitable preconditioning matrix P_c. We used the formulation proposed by (Turkel 1987) with the primitive variables pressure, velocity and entropy :

$$P_c = \begin{bmatrix} \beta^2 & 0 & 0 \\ 0 & 1 & 0 \\ 0 & 0 & 1 \end{bmatrix}$$

β is a parameter of the order of the Mach number. In our study, we have chosen the form given by (Choi and Merkle 1993):

$$\beta^2 = \min\left[\max\left(M^2, KM_\infty^2\right), 1\right] \tag{7}$$

This form implies that there is no preconditioning used in transonic and supersonic flow regions (in the mixture). When $\beta^2 = 1$, the preconditioning matrix becomes the identity matrix and the system returns to its classical non-preconditioned form. Moreover, for very small flow-velocity, β^2 is not allowed to be less than a given percentage of the freestream velocity, determined by the coefficient K. For inviscid computations, K is near unity.

4.2 *The compressible RANS system*

The inviscid preconditioner presented previously is used (no viscous terms are introduced). The compressible RANS equations coupled with a two-equation turbulence model can be expressed as:

$$P_c^{-1}\frac{\partial W}{\partial t} + \operatorname{div}(F_c - F_v) = S \tag{8}$$

$$W = \begin{pmatrix} \rho \\ \rho V \\ \rho E \\ \rho k \\ \rho \Psi \end{pmatrix} \quad ; \qquad F_c = \begin{pmatrix} \rho V \\ \rho V \otimes V + P\overline{\overline{I}} \\ (\rho E + P)V \\ \rho k V \\ \rho \Psi V \end{pmatrix} \quad ; \qquad F_v = \begin{pmatrix} 0 \\ \overline{\overline{\tau}} \\ \overline{\overline{\tau}}.V - q \\ (\mu + \mu_t/\sigma_k)\operatorname{grad} k \\ (\mu + \mu_t/\sigma_\Psi)\operatorname{grad} \Psi \end{pmatrix}$$

where W denotes the conservative variables, V the mean velocity vector, E the total energy, F_c and F_v the convective and viscous flux densities and S the source terms which concern only the transport equations. Ψ is a turbulent variable.
The exact expression of the eddy viscosity μ_t and the source terms depends on the turbulence model as well as constants σ_k and σ_Ψ. $\overline{\overline{\tau}}$ is the total stress tensor and q the total heat flux vector, evaluated with the Newtonian law, the Fourier law and the Boussinesq assumption.
For pure phases, we use the convex stiffened gas equation of state (Le Metayer *et al.* 2004) :

$$P(\rho, e) = (\gamma - 1)\rho(e - q_{ref}) - \gamma P_\infty \tag{9}$$

$$P(\rho, T) = \rho(\gamma - 1)C_v T - P_\infty \tag{10}$$

$$T(\rho, h) = \frac{h - q_{ref}}{C_p} \tag{11}$$

where $\gamma = C_p/C_v$ is the polytropic coefficient, C_p and C_v are thermal capacities, q_{ref} the energy of the fluid at a given reference state and P_∞ a constant reference pressure. e and h denote the internal energy and enthalpy respectively.

4.3 *Spatial discretization*

Using the finite-volume technique for space discretization, a semi-discrete form of equation (8) may be written for a computational cell of volume Ω limited by a surface Σ and with an outer normal n:

$$P_c^{-1}\Omega\frac{\partial W}{\partial t} + \sum_{all\,faces} (F_c - F_v).n\Sigma = \Omega\hat{S} \tag{12}$$

For the mean flow, the convective flux density vector on a cell face is computed with the space-centered Jameson scheme stabilized by scalar artificial dissipation (Jameson *et al.* 1981).

Discretization of the viscous terms is performed by a second-order space-centered scheme.
For the turbulence transport equations, the upwind Roe scheme (Roe 1981) was used to obtain a more robust method. The second-order accuracy was obtained by introducing a flux-limited dissipation.

4.4 *Temporal discretization*

Time integration is achieved through a low-cost implicit method (Luo *et al.* 1998). The implicit method consists in solving, at each time step, a system of equations arising from the linearization of a fully implicit scheme. The main advantage of this method is that the storage of the Jacobian matrix is completely eliminated, which leads to a low-storage algorithm. The viscous flux Jacobian matrices are replaced by their spectral radii. The Jacobian matrices, which appear from the linearization of the centered fluxes, are approximated with the numerical fluxes. The following system is obtained, for iteration n:

$$\Delta W^n + \sum_{l=i,j,k} \left[\sigma_l \delta_l \mu_l(\Delta f_l^n) - \sigma_l \delta_l(\rho_l^V \Delta W^n) - 0.5\sigma_l \delta_l \left(P^{-1}\rho(PA_l)\delta_l \Delta W^n\right)\right] = R_{expl}^n \tag{13}$$

where $\Delta W^n = W^{n+1} - W^n$, $\sigma_l = \Delta t/\Delta x_l$, and R_{expl}^n represents the explicit conservative residuals. For each direction l, ρ_l^V is the viscous spectral radius, μ_l the averaged operator, δ_l the difference operator, A_l the Jacobian matrix of the convective flux for the direction l and $\rho(PA_l)$ the spectral radius of the matrix PA_l.

The implicit time-integration procedure leads to a system which can be solved directly or iteratively. The direct inversion can be memory intensive and computationally expensive. Therefore, an implicit relaxation procedure is preferred and the point Jacobi relaxation algorithm was chosen.

For unsteady computations, the dual time stepping method, proposed by (Jameson 1991), was used to tackle the lack of numerical efficiency of the global time stepping approach. The derivative with respect to the physical time is discretized by a second-order formula. The initialization of the derivative with respect to the physical time was performed with a first-order formula.

4.5 *Turbulence modelling*

The considered model is the Jones-Launder $k-\varepsilon$ model (Jones and Launder 1972). In two-phase areas, the Reboud limiter is applied with the same constant $n = 10$. The turbulence model is coupled with standard wall functions. Computations with both codes were not performed rigorously with the same turbulence model, but we assumed that the Jones-Launder and the RNG $k-\varepsilon$ models roughly provided similar solutions.

4.6 *Inlet and outlet boundary conditions*

The numerical treatment of the boundary conditions is based on the use of the preconditioned characteristic relations. The number of variable to impose at boundaries is given by the number of positive characteristics. The characteristic relations obtained for the preconditioned system, in two-dimensional flows, are:

$$-c^2(\rho^c - \rho^s) + (P^c - P^s) = 0 \tag{14}$$

$$V_t^c - V_t^s = 0 \tag{15}$$

$$(\lambda_+ - V_n)(P^c - P^s) + \rho\beta^2 c^2(V_n^c - V_n^s) = 0 \tag{16}$$

$$(\lambda_- - V_n)(P^c - P^s) + \rho\beta^2 c^2(V_n^c - V_n^s) = 0 \tag{17}$$

The variables with superscript c are those to be computed at the boundary. Variables with superscript s are obtained by the current numerical scheme. V_t and V_n are the tangential and normal components of the mean velocity respectively. λ_+ and λ_- are the eigenvalues of the preconditioned inviscid system, given by:

$$\lambda_\pm = \frac{1}{2}\left[u(1+\beta^2) \pm \sqrt{(\beta^2-1)^2u^2 + 4\beta^2c^2}\right] \tag{18}$$

At inflow, four variables have to be imposed. We have chosen the stagnation pressure P_i, the stagnation temperature T_i, and the direction of the velocity. A Newton algorithm can be used to compute the pressure with the characteristic relation (17) and the conservative variables can be evaluated at the boundary.
At outflow, only one variable is imposed, which we have chosen to be the static pressure. The conservative variables are computed with three characteristic relations (14)-(16).
We assume that inlet and outlet areas are in a pure liquid region. No cavitation appears in these boundaries.

5 COMPUTATIONS AND COMPARISONS: OPEN CAVITY

The first case is an open cavity on a Venturi geometry, following the classification of partial cavity flows (Laberteaux and Ceccio 2001).

5.1 *Experimental geometry and conditions*

The tested Venturi is characterized by a divergence angle of 4° (see Figure 2). The selected operating point is characterized by (Barre *et al.* 2009):
$U_{inlet} = 10.8$ m/s : the inlet velocity
$P_{inlet} = 35000$ Pa : the pressure in the inlet section
$T_{ref} = 293K$: the reference temperature
$\sigma_{inlet} = \dfrac{P_{inlet} - P_{vap}}{0.5\rho U_{inlet}^2} \simeq 0.55$: the cavitation parameter in the inlet section
$Re_{L_{ref}} = \dfrac{U_{inlet} L_{ref}}{\nu} = 2.710^6$: the Reynolds number
With these parameters, a cavity length L ranging between 70 mm and 85 mm has been obtained.

The experimental void ratio and velocity profiles are obtained for five stations by a double optical probe (Figures 2 and 3). The velocity is evaluated as the most probable value and the void ratio is obtained from the signal of the double optical probe using a post processing algorithm.

The experimental views for this geometry show a relatively stable cavity behaviour (Figure 4). It is characterized by an almost constant length, although the closure region always fluctuates, with the existence of a re-entrant jet and little vapour cloud shedding. The re-entrant jet is mainly composed of liquid which flows upstream along the solid surface. For this geometry, no periodic cycles with large shedding were observed.

5.2 *Mesh*

The grid is an H-type topology. It contains 251 nodes in the flow direction and 62 in the orthogonal direction. A special contraction of the mesh is applied in the main flow direction just after the throat to better simulate two-phase flow area (Figure 5). The y^+ values of the mesh, at the center of the first cell, vary between 12 and 27, for a non-cavitating computation.

According to the study of mesh dependence presented in (Coutier-Delgosha *et al.* 2005), this grid size is adequate to simulate cavitation sheets in such Venturi type section.

5.3 *Numerical parameters*

For the non-cavitating regime, computations are started from an uniform flow-field. For the cavitating regime, we used for both codes :
- the vapour pressure, $P_{vap} = 2339Pa$
- the saturation values of liquid/vapour density, $\rho_L^{sat} = 1000kg/m^3$ and $\rho_V^{sat} = 0.02kg/m^3$
- the farfield value of turbulent kinetic energy, k_∞=0.0045 m^2/s^2
- the dimensionless time step for unsteady computations, $\Delta t^* = \dfrac{\Delta t U_{inlet}}{L_{ref}} = 0.015$.

The numerical parameters used for simulations are summarized in Table (1) and Table (2).

5.4 *Comparison of the two solvers*

Two series of solutions are presented and compared: steady and unsteady solutions.

5.4.1 Steady solutions

First, the goal was to obtain a steady solution with a stable cavitation sheet with a length close to 80 mm. The defined sheet length L_{cav} used for representing the computational results has been determined by the length of the iso-line corresponding to a void ratio $\alpha = 0.2$.
With the compressible solver, steady computations were carried out with a local time stepping method whereas, with the incompressible solver, unsteady simulations were performed without reducing the turbulent viscosity. The overall results are given in Table (3). The σ_{inlet} value obtained with the compressible code is over-estimated in comparison with both the experimental value and the numerical "incompressible" value.

Figure 6 shows the longitudinal velocity (left) and void ratio (right) profiles for the present experiments and numerical simulations. The overall agreement seems good between the experimental data and simulations. This is especially true for stations 1 and 2 where no re-entrant jet phenomena occur. Further downstream, experimental observation indicates a recirculating behaviour with a re-entrant jet extending roughly through half the sheet thickness. No relevant influence of the numerical schemes and turbulence models is observed.

The wall pressure profiles are plotted in Figure 7 versus the distance $x - x_{inlet}$. The first five data are located inside the cavity (where void ratio and velocity profiles are measured). For all computations, the pressure remains at an almost constant value in the cavity. Downstream, discrepancies are notable due to the re-entrant jet. In comparison with experimental data, the re-compression is a little under-evaluated with the compressible code and over-estimated with the incompressible code.

5.4.2 Unsteady solutions

Next, unsteady calculations were performed with the goal of obtaining a quasi-stable cavitation sheet with a significant re-entrant jet. With the compressible solver, unsteady computations were carried out with the dual time stepping method and the Reboud viscosity limiter. With the incompressible solver, unsteady simulations were performed with the same turbulent viscosity limiter. The overall results are given in Table 4; they show the better agreement obtained with the compressible code for the σ_{inlet} value.

The numerical solutions obtained from both codes present some marked differences. The incompressible code captured low frequency periodic oscillations of the cavitating sheet (around

6 Hz). A view of the cavity (contours of the void ratio) obtained with the IZ code over one period is presented in Figure 8. Oscillations of the cavity are clearly exhibited.
On the other hand, the compressible code captured a quasi-stable behaviour in good agreement with the experimental view. No frequencies are revealed by a direct Fourier transformation of the vapour volume. A view of the cavity at five instants is plotted in Figure 9. We can observe the attached cavity from the throat of the Venturi up to $x = 0.3$m. Downstream, the recirculating area with two-phase structure shedding is well illustrated.

Figure 10 shows the longitudinal velocity (left) and void ratio (right) profiles for experiments and unsteady numerical results. The numerical values are obtained by a time-averaged treatment.

At stations 3, 4 and 5, the recirculating behaviour with a re-entrant jet is well simulated by the compressible code. On the other hand, the incompressible code largely under-estimated the re-entrant jet intensity and the thickness of the recirculating area (at station 3, it is not captured).
For the void ratio profiles, both codes provided a similar solution at station 3, in good agreement with the experimental data. At station 4, with the incompressible code, a liquid re-entrant jet ($\alpha = 0$) is observed close to the wall, up to a distance $y = 0.001$m, whereas the re-entrant jet captured by the compressible calculation is not composed of pure liquid (at the wall, the void ratio value is around 0.35 instead of 0.15). At station 5, the length of the sheet obtained with the incompressible code is shorter than the experimental value. With the compressible code, the void ratio is in very close agreement with the experimental data.

The wall pressure is plotted in Figure 11 versus the distance $x - x_{inlet}$. Theses values are obtained by a time-averaged treatment for both experiments and calculations.
With the incompressible code, the computed pressure inside the cavity is smaller than the vapour pressure. After station 3, we observe an area where the time-averaged pressure is above the vapour pressure, due to the oscillating behaviour of the cavity. With the compressible code, the pressure inside the cavity is in good agreement with the experimental data. Downstream, the re-compression is slightly under-evaluated, as previously observed with the steady simulations.

Comparisons with measurements data suggest that the compressible formulation provides an improved description of the cavitation dynamics compared with incompressible computations.

6 COMPUTATIONS AND COMPARISONS: UNSTEADY RE-ENTRANT CAVITY

The second case is an unsteady re-entrant cavity with quasi periodic break-off and roll-up of a portion of the cavity.

6.1 *Experimental geometry and conditions*

This Venturi is characterized by a divergence angle of 8°, illustrated in Fig. 12. The geometrical data are:
Inlet section: $S_i = 50 \times 44$ mm^2 (where the reference pressure is measured);
Throat section: $S_{throat} = 33.5 \times 44$ mm^2;
Length of the test section (chord): $L_{ref} = 224$ mm.

The selected operating point is characterized by the following physical parameters debined by Fortes-Patella *et al.* (2006):
$U_{inlet} = 7.04$ m/s: the inlet velocity
$Q = 0.0155$ m^3/s: the flow imposed in the circuit

$P_{inlet} = 55000$ Pa: the pressure in the inlet section
$\sigma_{inlet} = \dfrac{P_{inlet} - P_{vap}}{0.5\rho U_{inlet}^2} \simeq 2.15 \pm 0.06$: the cavitation parameter in the inlet section
$Re_{L_{ref}} = \dfrac{U_{inlet} L_{ref}}{\nu} = 1.57\,10^6$: the Reynolds number
With these parameters, an unsteady cavity with quasi-periodic fluctuations of the attached sheet and vapour clouds shedding has been obtained. Fig. 13 shows an instantaneous photograph of the cavity with a large structure shedding. The maximum length L of the attached cavity is about 45 mm. The vapour shedding frequency is close to 45 Hz, estimated from Fourier transformations of the unsteady pressure signal.

This geometry is equipped with three probing holes to make various measurements such as the local void ratio and instantaneous local velocity (Fig. 14).

6.2 *Mesh*

The grid is an H-type topology. It contains 250 nodes in the flow direction and 61 in the orthogonal direction. A special contraction of the mesh is applied in the main flow direction just after the throat to better simulate the two-phase flow area (Fig. 15). The y^+ values of the mesh, at the center of the first cell, vary between 9 and 31 for a non cavitating computation.

6.3 *Numerical parameters*

For the cavitating regime, the dimensionless time step is: $\Delta t^* = \dfrac{\Delta t U_{inlet}}{L_{ref}} = 6\,10^{-3}$.

Numerical parameters used for simulations are similar to those presented previously.

6.4 *Global analyses*

Different calculations were performed, summarized in Table (5). The goal was to obtain a periodic cavitation sheet with a frequency close to 45 Hz.

The vapour volume changes are plotted in Fig. 16 for both codes. The incompressible solution seems more regular. Moreover, the values are quite different: the ratio between compressible and incompressible values is around 2.
A direct Fourier transformation (DFT) of the vapour volume was performed to evaluate the frequency. Fig. 17 presents the frequency results for the incompressible code (left) and the compressible code (right). A peak is clearly visible for both codes, with better agreement for the incompressible code.

A view of the cavity (contours of the void ratio) obtained with the incompressible IZ code, over one period, is presented in Figure 18. Large-scale two-phase structure shedding is clearly observed. The re-entrant jet is very intense and flows upstream to the throat of the Venturi, leading to the disappearance of the attached cavity. These results corroborate conclusions presented in (Venkateswaran *et al.* 2002).

The solution obtained with the compressible code presents differences. A view of the cavity over one period is plotted in Figure 19. A small cavity attached to the throat is always present. Two-phase structures convected in the flow are smaller and condense rapidly, in comparison with the incompressible solution.

6.5 *Velocity and void ratio profiles*

Figure 20 illustrates the longitudinal velocity (left) and void ratio (right) profiles for experiments and unsteady numerical results. The numerical values are obtained by a time-averaged treatment.

At station 1, with the compressible code, the recirculating behaviour is very well captured, yet the void ratio is largely over-predicted. For the incompressible code, the void ratio is slightly under-estimated due to the disappearance of the attached cavity.
At station 2, both codes under-evaluated the recirculating zone thickness. For the void ratio profile, values obtained with the incompressible code are largely over-predicted, whereas values obtained by the compressible code are in better agreement with the experimental data.
At station 3, no experimental velocity profiles are usable. For the void ratio profile, the compressible code computed a pure liquid zone: two-phase structures shedding is not enough extended. On the other hand, the incompressible code captured large-scale cavitation structures, but with excessive void ratio values.

7 CONCLUSION

Two different cavitating one-fluid CFD code have been presented and applied to Venturi flows. The first is based on a pressure-based incompressible algorithm modified to take into account density variations. The second uses a density-based compressible approach including a preconditioning algorithm to treat the pure liquid incompressible region.
Both codes were compared on cavitating flows using the same cavitation model, the same mesh, a $k-\varepsilon$ model with the same viscosity limiter and the same numerical time step. Two different cavitation cases were tested: an aperiodic quasi-stable cavity sheet and a quasi-periodic unsteady re-entrant cavity. Global and local analysis of flows based on void ratio and velocity profiles were carried out.
For the first case, the compressible code captured a solution in close agreement with the experimental data, both for the global behaviour and the local analysis. On the other hand, the incompressible code provided a different solution with a periodic low frequency oscillating sheet. For this case, it seems necessary to account for compressibility effects to correctly describe the cavity dynamics.
For the second case, the re-entrant jet phenomenon obtained with both codes presents some marked differences. The compressible code under-predicted large-scale cavitation structure shedding. The opposite situation is observed with the incompressible code: a very intense re-entrant jet is captured, which flows upstream to the throat and completely eliminates the attached cavity. These results corroborate conclusions presented in (Venkateswaran *et al.* 2002).
Additional investigations are necessary to clearly conclude on the importance of the compressibility effects. Additional computations are in progress to analyze the influence of the turbulence model for unsteady computations and to pursue comparative studies between numerical approaches.

References

Ahuja, V., Hosangadi, A., and Arunajatesan, S., 2001. Simulations of cavitating flows using hybrid unstructured meshes. *Journal of Fluids Engineering*, 123(2), 331-340.

Barre, S., Rolland, J., Boitel, G., Goncalves, E., and Fortes Patella, R., 2009. Experiments and modelling of cavitating flows in Venturi: attached sheet cavitation. *European Journal of Mechanics B/Fluids*, 28, 444–464.

Choi, YH., and Merkle, CL., 1993. The application of preconditioning to viscous flows. *Journal of Computational Physics*, 105(2), 207–223.

Coutier-Delgosha, 0., Fortes-Patella, R., and Reboud, J-L., 2002. Simulation of unsteady cavitation with a two-equation turbulence model including compressibility effects. *Journal of Turbulence*, 3(58).

Coutier-Delgosha, 0., Reboud, J-L., and Delannoy, Y., 2003. Numerical simulation of the unsteady behaviour of cavitating flow. *Int. Journal for Numerical Methods in Fluids*, 42, 527–548.

Coutier-Delgosha, 0., Fortes-Patella, R., Reboud, J-L., Delannoy, Y., N. Hakimi and C. Hirsch, 2005. Numerical simulation of cavitating flow in 2D and 3D inducer geometries. *Int. Journal for Numerical Methods in Fluids*, 48, 135–167.

Delannoy, Y., and Kueny, J-L., 1990. Two phase flow approach in unsteady cavitation modelling. *Cavitation and Multiphase Flow Forum, ASME-FED*, 98, 153–158.

Edwards, JR., and Franklin, RK., 2000. Low-Diffusion Flux Splitting methods for real fluid flows with phase transition. *AIAA Journal*, 38(9), 1624–1633.

Fortes-Patella, R., Barre, S., and Reboud, J-L., 2006. Experiments and modelling of cavitating flows in Venturi : part II, unsteady cavitation. *6th International Symposium on Cavitation CAV2006*, Wageningen, The Netherlands, September 11-15, 2006.

Goncalves, E., and Fortes-Patella, R., 2009. Numerical Simulation of Cavitating Flows with Homogeneous Models. *Computers & Fluids*, 38(9), 1682–1696.

Housman, J., Kiris, C., and Hahez, M., 2009. Preconditioned methods for simulations of low speed compressible flows. *Computers & Fluids*, 38(7), 1411–1423.

Jameson, A., Schmidt, W., and Turkel, E., 1981. Numerical simulation of the Euler equations by finite volume method using Runge-Kutta time stepping schemes. AIAA paper 81-1259, *14th Fluid and Plasma Dynamics Conference*, Palo Alto, California, 1981.

Jameson, A., 1991. Time Dependent Calculations Using Multigrid with Applications to Unsteady Flows past Airfoils and Wing. AIAA paper 91-1259, *10^{th} Computational Fluid Dynamics Conference*, Honolulu, Hawai, 1991.

Jones, W.P., and Launder, B.E., 1972. The Prediction of Laminarization with a Two-Equation Model of Turbulence. *Int. J. Heat Mass Transfer*, 15, 301–314.

Kunz, RF., Boger, DA., Stinebring, DR., Chyczewski, TS., Lindau, JW., Gibeling, HJ., Venkateswaran, S., and Govindan, TR., 2000. A preconditioned Navier-Stokes method for two-phase flows with application to cavitation prediction. *Computers & Fluids*, 29(8), 849–875.

Laberteaux, K.R., and Ceccio, S.L., 2001. Partial cavity flows. Part1. Cavities forming on models without spanwise variation. *J. Fluid Mech.*, 431, 1–41.

Liu, TG., Khoo, BC., and Xie, WF., 2004. Isentropic one-fluid modelling of unsteady cavitating flow. *Journal of Computational Physics*, 201(1), 80–108.

Luo, H., Baum, J.D., and Lohner, R., 1998. A fast, matrix-free implicit method for compressible flows on unstructured grids. *Journal of Computational Physics*,146, 664–690.

Le Metayer, O., Massoni, J., and Saurel, R., 2004. Elaborating equations of state of a liquid and its vapor for two-phase flow models. *Int. Journal of Thermal Sciences*, 43, 265–276.

Moreau, JB., Simonin, O., and Habchi, C., 2004. A numerical study of cavitation influence on diesel jet atomisation. *19th annual meeting of the institute for liquid atomization and spray systems*, Notthingham, England, 2004.

Patankar, S.V., and Spalding, D.B., 1972. A calculation procedure for heat, mass and momentum transfer in three-dimensional parabolic flows. *Int. Journal for Heat and Mass Transfer*, 15, 1787–1795.

Pouffary, B., Fortes Patella, R., Reboud, J-L., and Lambert, PA., 2008. Numerical simulation of 3D cavitating flows: analysis of cavitation head drop in turbomachinery. *Journal of Fluids Engineering*, 130(6), 061301.

Reboud, J-L., Stutz, B., and Coutier, O., 1998. Two-phase flow structure of cavitation: experiment and modelling of unsteady effects. *3^{rd} International Symposium on Cavitation CAV1998*, Grenoble, France, 1998.

Roe, P.L., 1981. Approximate Riemann solvers, parameters vectors, and difference schemes. *Journal of Computational Physics*, 43, 357–372.

Rossow, C-C., 2007. Efficient computation of compressible and incompressible flows. *Journal of Computational Physics*, 220(2), 879–899.

Schmidt, SJ., Sezal, IH., and Schnerr, GH., 2006. Compressible simulation of high-speed hydrodynamics with phase change. *European Conference on Computational Fluid Dynamics ECCOMAS2006*, Delft, The Netherlands, 2006.

Senocak, I., and Shyy, W., 2002. A pressure-based method for turbulent cavitating flow computations. *Journal of Computational Physics*, 176(2), 363–383.

Singhal, AK., Athavale, MM., Li, H., and Jiang, Y., 2002. Mathematical basis and validation of the full cavitation model. *Journal of Fluids Engineering*, 124(3), 617–624.

Sinibaldi, E., Beux, F., and Salvetti, MV., 2006. A numerical method for 3D barotropic flows in turbomachinery. *Flow Turbulence Combustion*, 76, 371–381.

Song, CS., 2002. Current status of CFD for cavitating flows. *9th International Symposium on Transport Phenomena and Dynamics of Rotating Machinery*, Honolulu, Hawai, 2002.

Turkel, E., 1987. Preconditioned methods for solving the incompressible and low speed compressible equations. *Journal of Computational Physics*, 172(2), 277–298.

Venkateswaran, S., Lindau, JW., Kunz, RF., and Merkle, CL., 2002. Computation of multiphase mixture flows with compressibility effects. *Journal of Computational Physics*, 180(1), 54–77.

Ventikos, Y., and Tzabiras, G., 2000. A numerical method for the simulation of steady and unsteady cavitating flows. *Computers & Fluids*, 29(1), 63–88.

Wu, J., Wang, G., and Shyy, W., 2005. Time-dependent turbulent cavitating flow computations with interfacial transport and filter-based models. *Int. Journal for Numerical Methods in Fluids*, 49(7), 739–761.

Yakhot, V., Orszag, S.A., Thangam, S., Gatski, T.B., and Speziale, C.G., 1992. Development of turbulence models for shear flows by a double expansion technique. *Physics of Fluids*, 4, 1510–1520.

Zhu, J., 1991. A low diffusive and oscillation-free convection scheme. *Communications in Applied Numerical Methods*, 7, 225–232.

List of Figures

List of Tables

Table2: Numerical parameters, CaviFlow

Table3: Sigma inlet values, steady solutions, 4° Venturi

Table4: Sigma inlet most probable values, unsteady solutions, 4° Venturi

Table5: Sigma inlet most probable values, unsteady solutions, 8° Venturi

Table 1. numerical parameters, IZ

IZ parameters	all computations
maximum of SIMPLE iterations / physical time step	1500
convergence criterion for the density ρ	10^{-6}
under-relaxation coefficient for ρ	0.2
under-relaxation coefficient for u and v	0.7
under-relaxation coefficient for k and ε	0.4

Table 2. numerical parameters, CaviFlow

CaviFlow parameters	steady non-cav	steady cav	unsteady cav
CFL number	10	0.5	0.5
preconditioning parameter K	1	3	3
implicit Jacobi iterations	15	15	15
2nd and 4th order dissipation parameter	0 ; 0.032	0.5 ; 0.040	0.5 ; 0.040
dual time stepping sub-iterations	-	-	100

Table 3. Sigma inlet values, steady solutions, 4° Venturi

	σ_{inlet}	L_{cav} (mm)
experimental	$\simeq 0.55$	$\simeq 80$
incompressible solver	0.585	80.1
compressible solver	0.63	78.9

Table 4. Sigma inlet most probable values, unsteady solutions, 4° Venturi

code	σ_{inlet}	L_{cav} (mm)	comments
incompressible solver	0.60	40 to 74	periodic oscillations of the sheet: 6Hz
compressible solver	0.56	70	quasi-stable sheet with re-entrant jet

Table 5. Sigma inlet most probable values, 8° Venturi

code	σ_{inlet}	comments
experimental	$\simeq 2.15$	periodic sheet: 45Hz
incompressible solver	2.11	periodic sheet: 48Hz
compressible solver	2.09	periodic sheet: 40 Hz

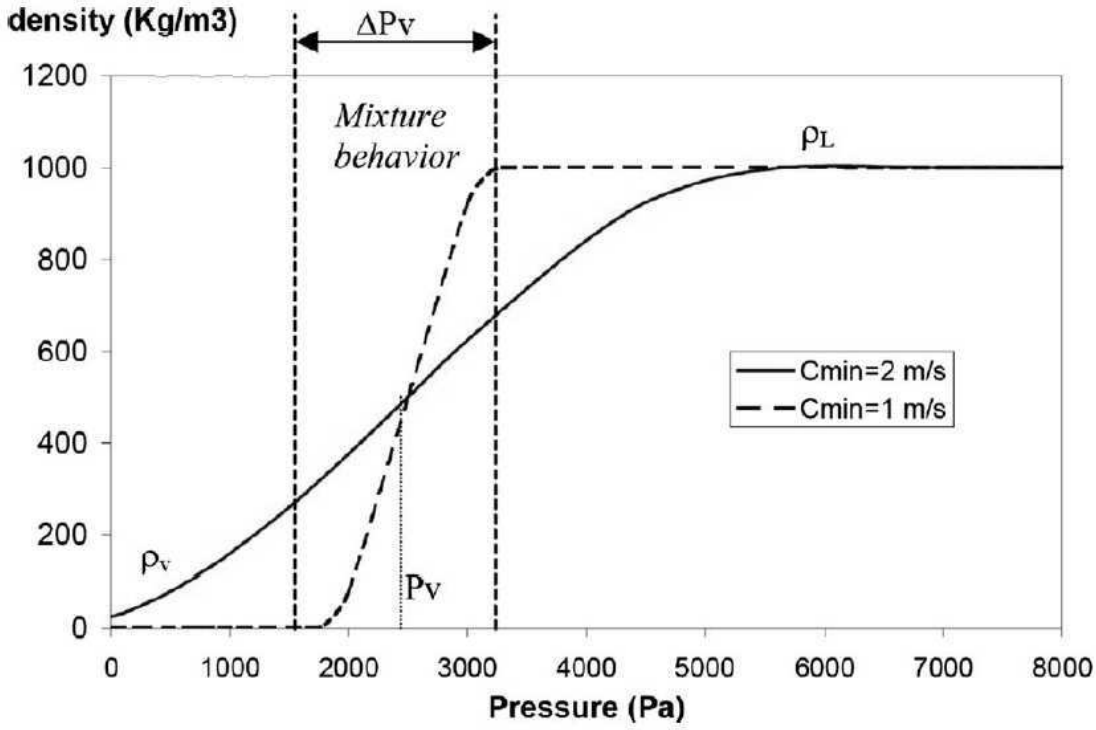

Figure 1. The barotropic equation of state

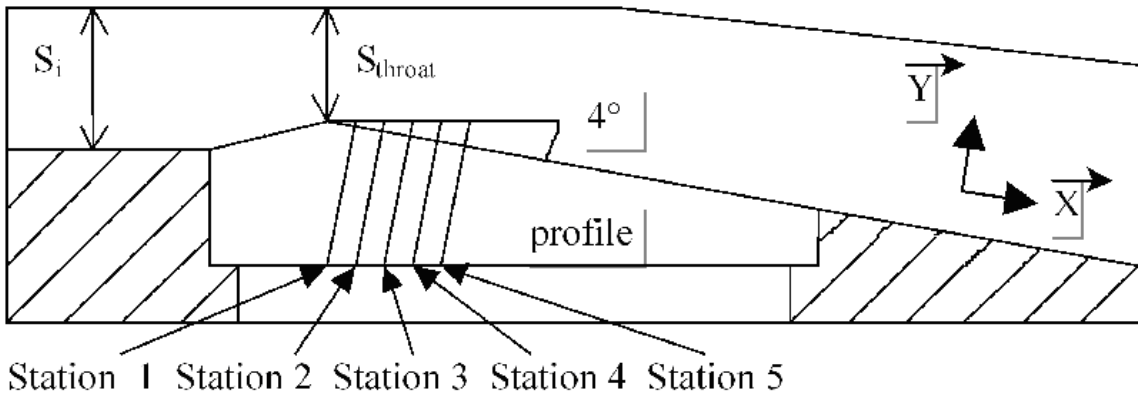

Figure 2. Schematic view of the 4° Venturi

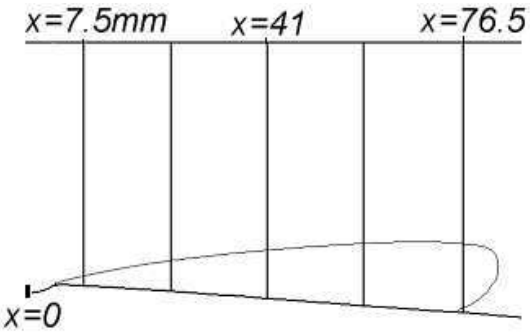

Figure 3. View of the cavity and the five stations, 4° Venturi

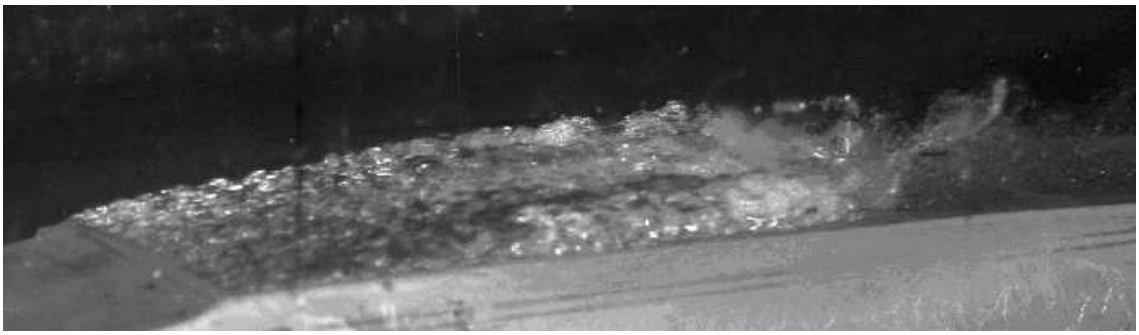

Figure 4. Photograph of the cavity, 4° Venturi

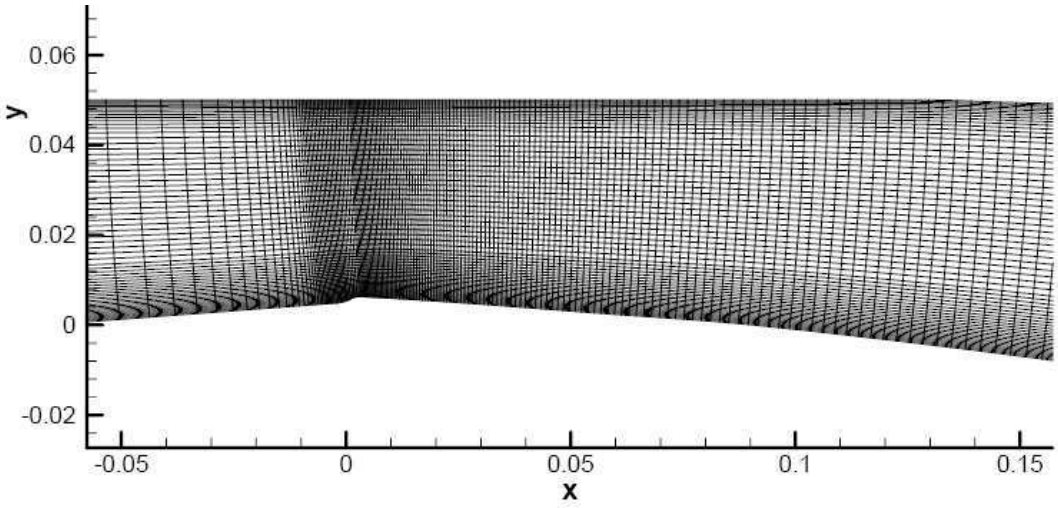

Figure 5. Enlargement of the mesh near the throat, 4° Venturi

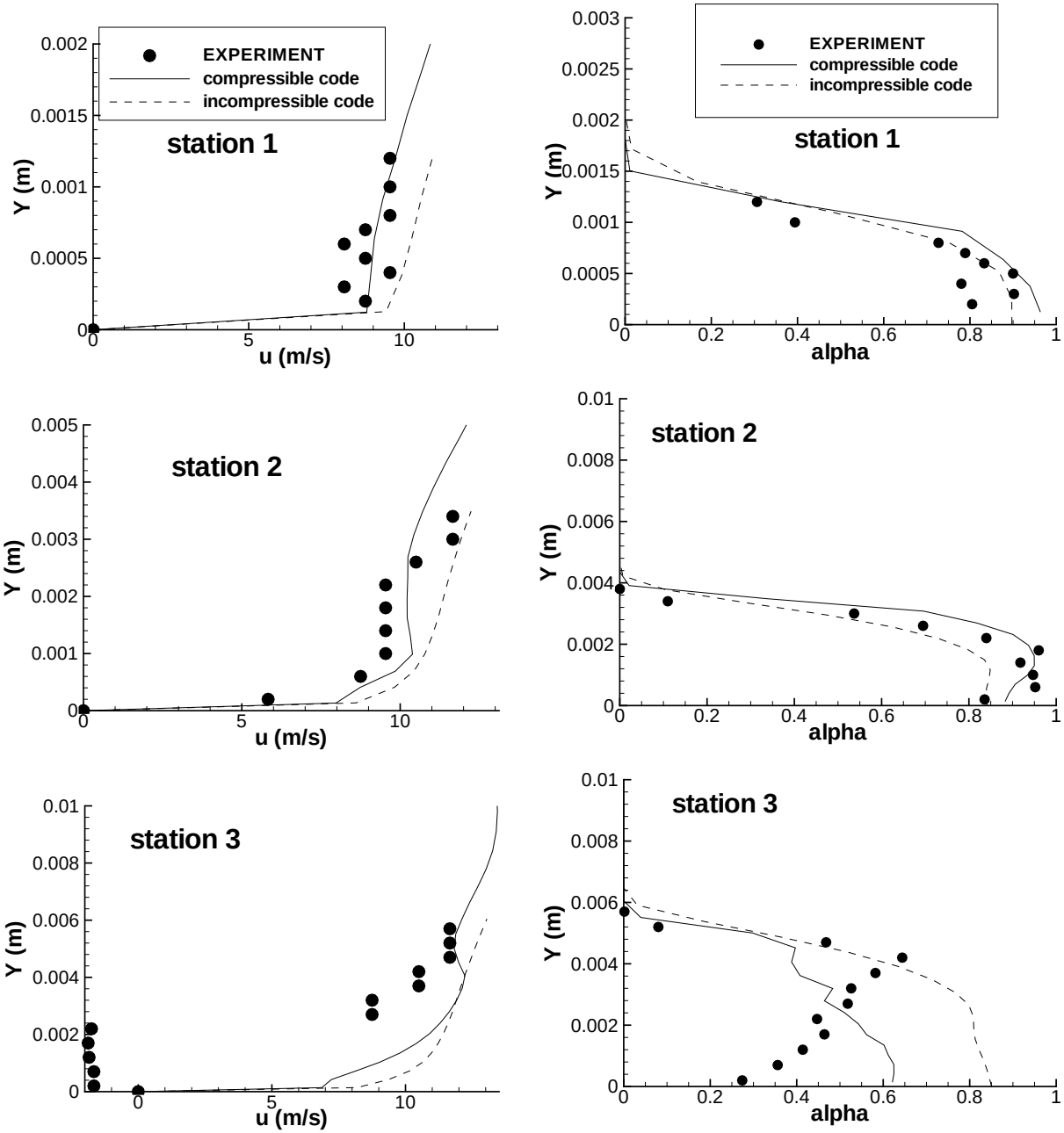

Figure 6. Velocity (left) and void ratio (right) profiles, steady solutions, 4° Venturi

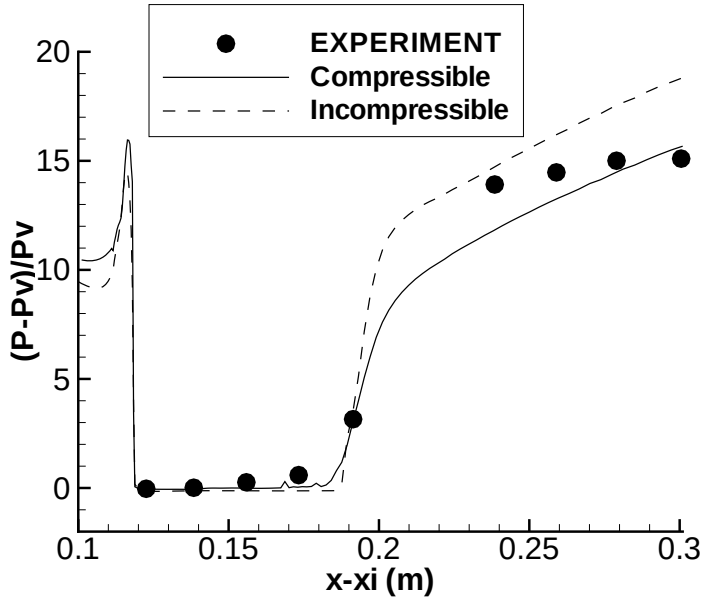

Figure 7. Wall pressure evolution, steady solutions, 4° Venturi

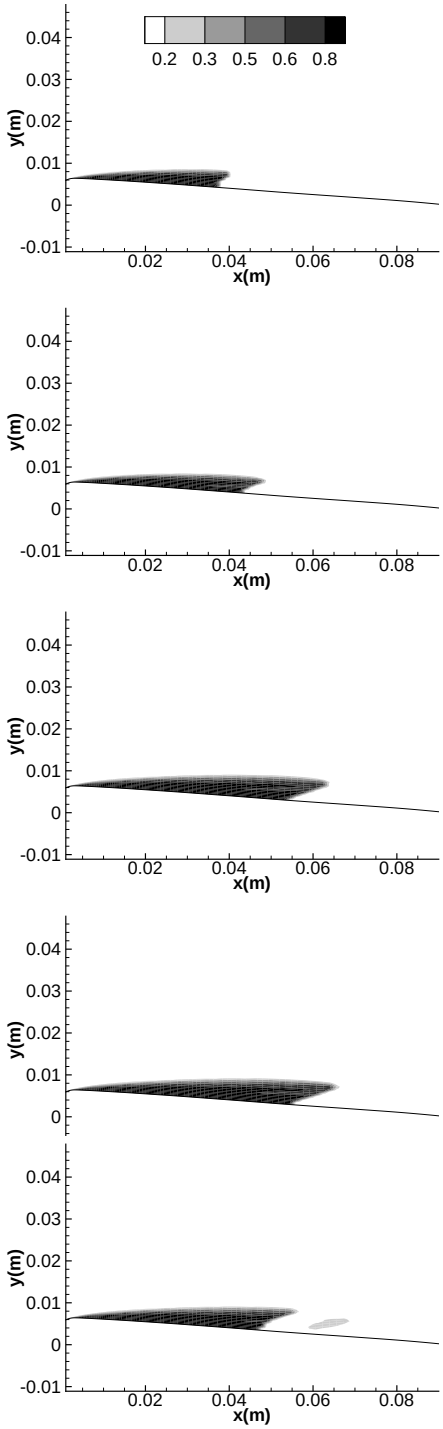

Figure 8. Contours of the void ratio over one period, incompressible code, 4° Venturi

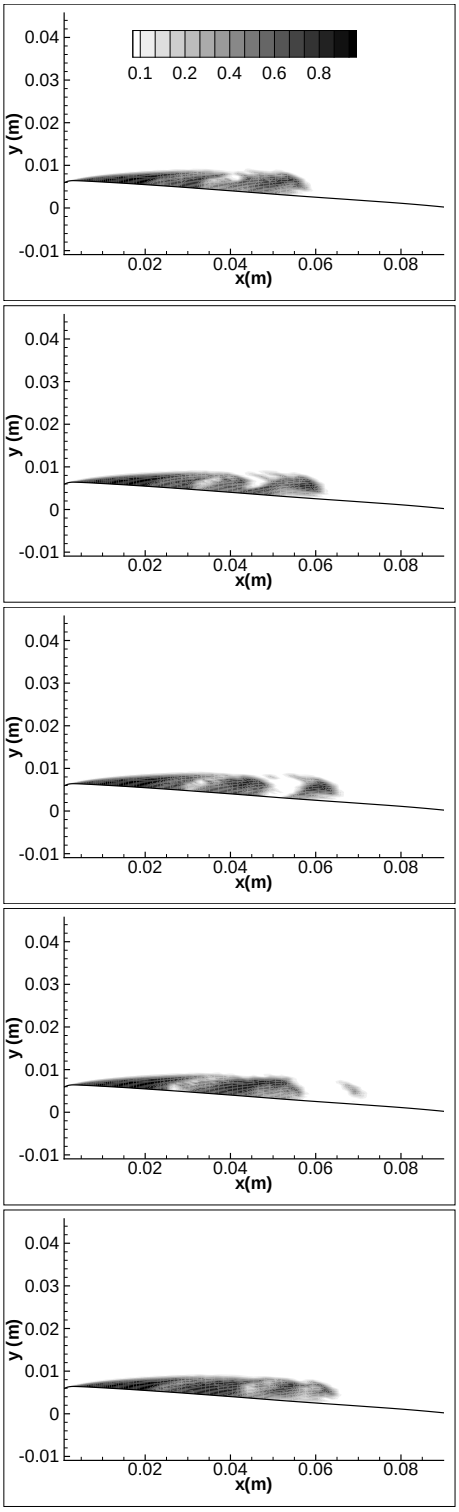

Figure 9. Contours of the void ratio at five instants, compressible code, 4° Venturi

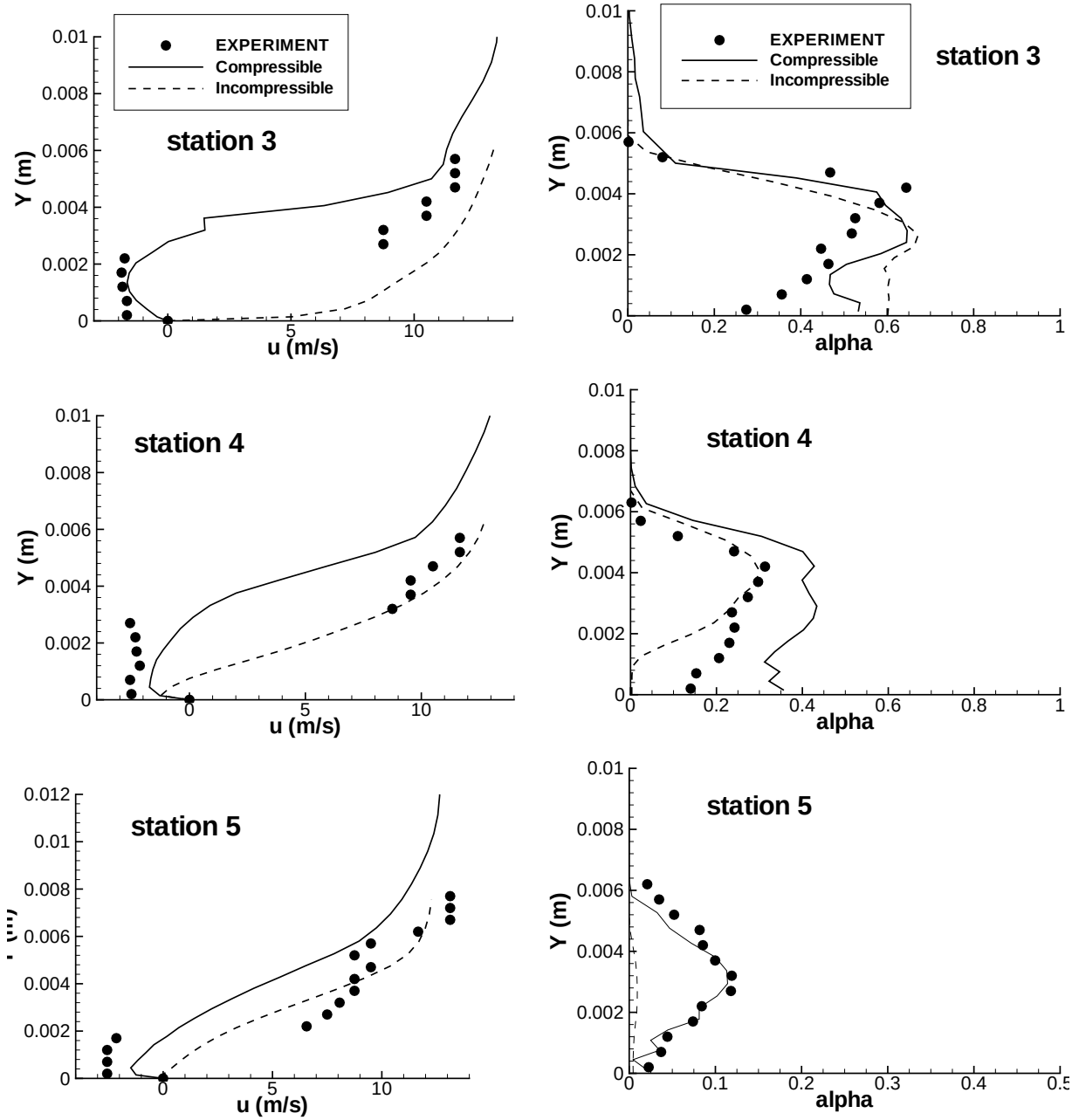

Figure 10. Time-averaged velocity (left) and void ratio (right) profiles, unsteady solutions, 4° Venturi

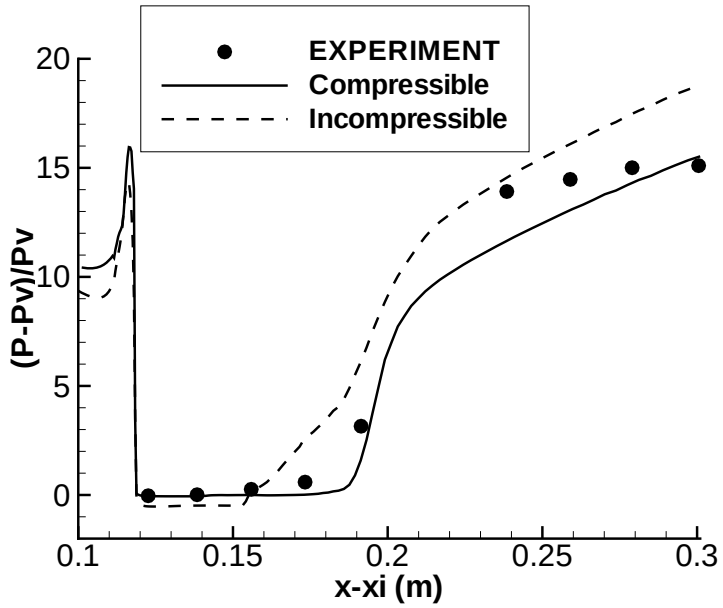

Figure 11. Time-averaged wall pressure evolution, unsteady solutions, 4° Venturi

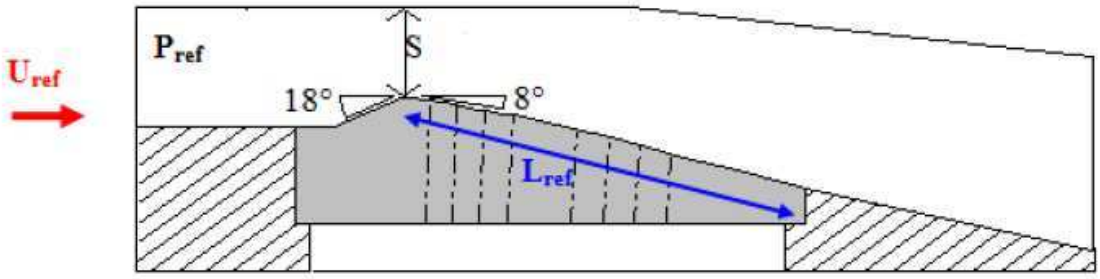

Figure 12. Schematic view of the 8° Venturi

Figure 13. Photograph of the cavity, 8° Venturi

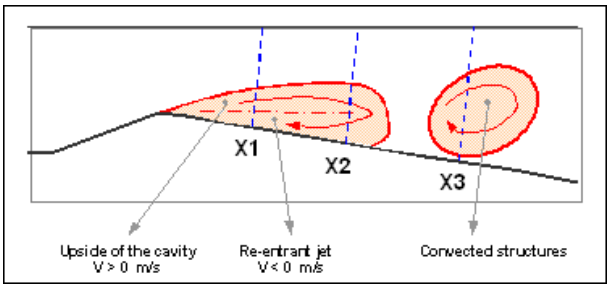

Figure 14. View of three stations of measurement, 8° Venturi

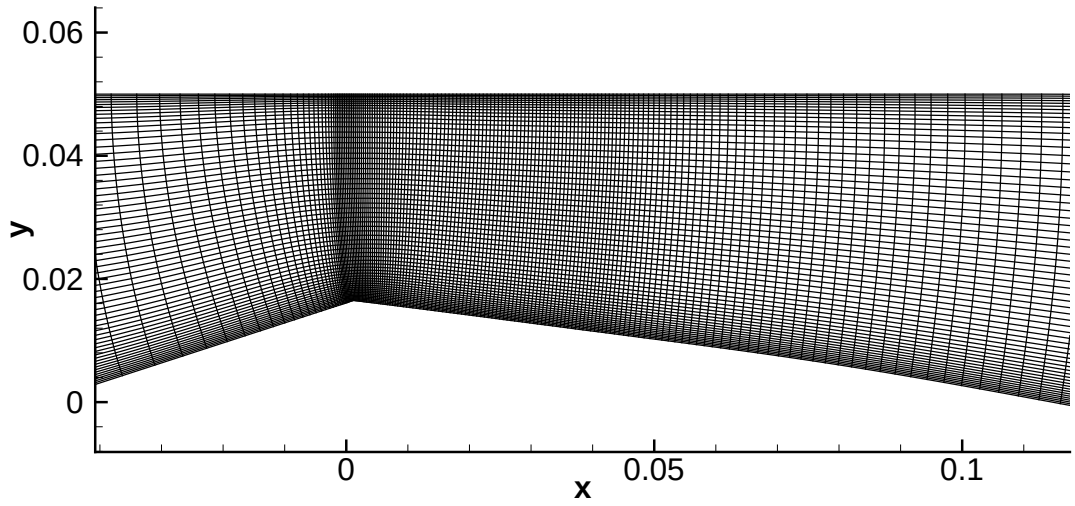

Figure 15. Enlargement of the mesh near the throat, 8° Venturi

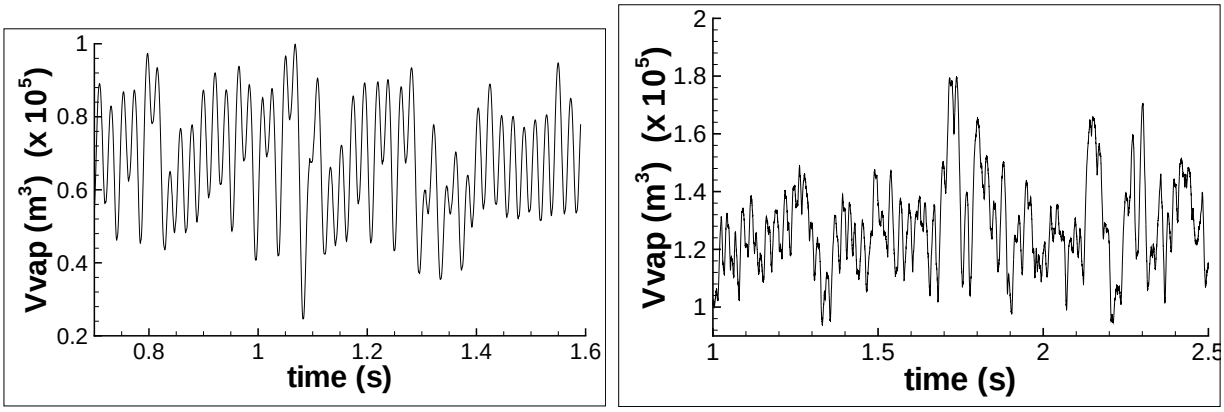

Figure 16. Evolution of the vapour volume, incompressible code (left) and compressible code (right), 8° Venturi

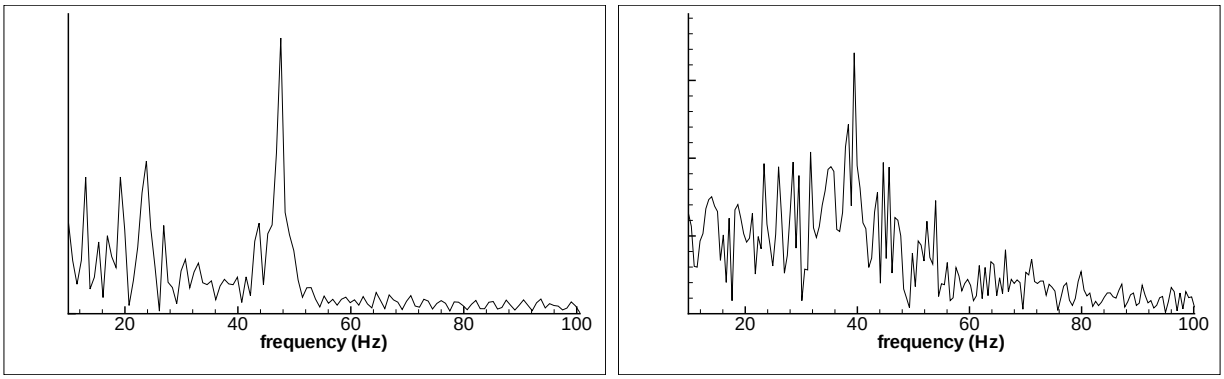

Figure 17. Fourier transformation of the vapour volume, incompressible code (left) and compressible code (right), 8° Venturi

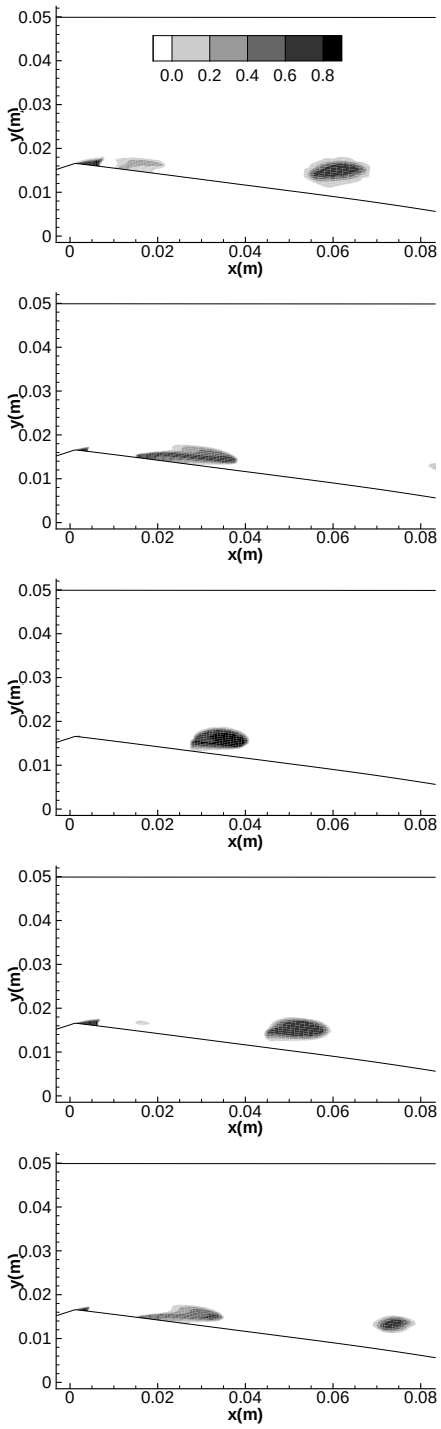

Figure 18. Contours of the void ratio over one period, incompressible code, 8° Venturi

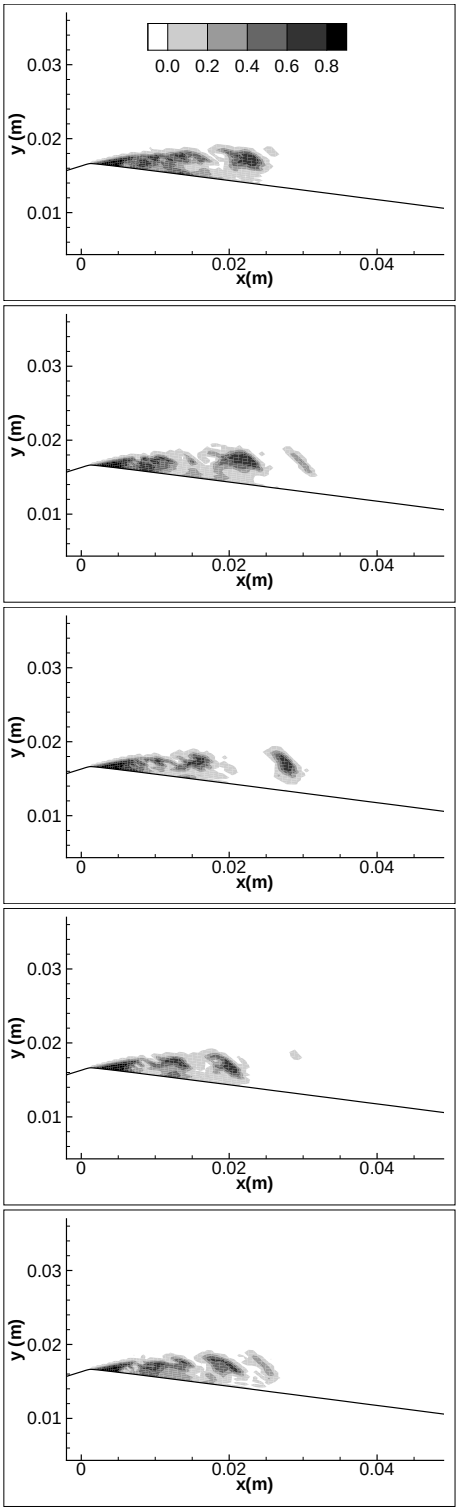

Figure 19. Contours of the void ratio over one period, compressible code, 8° Venturi

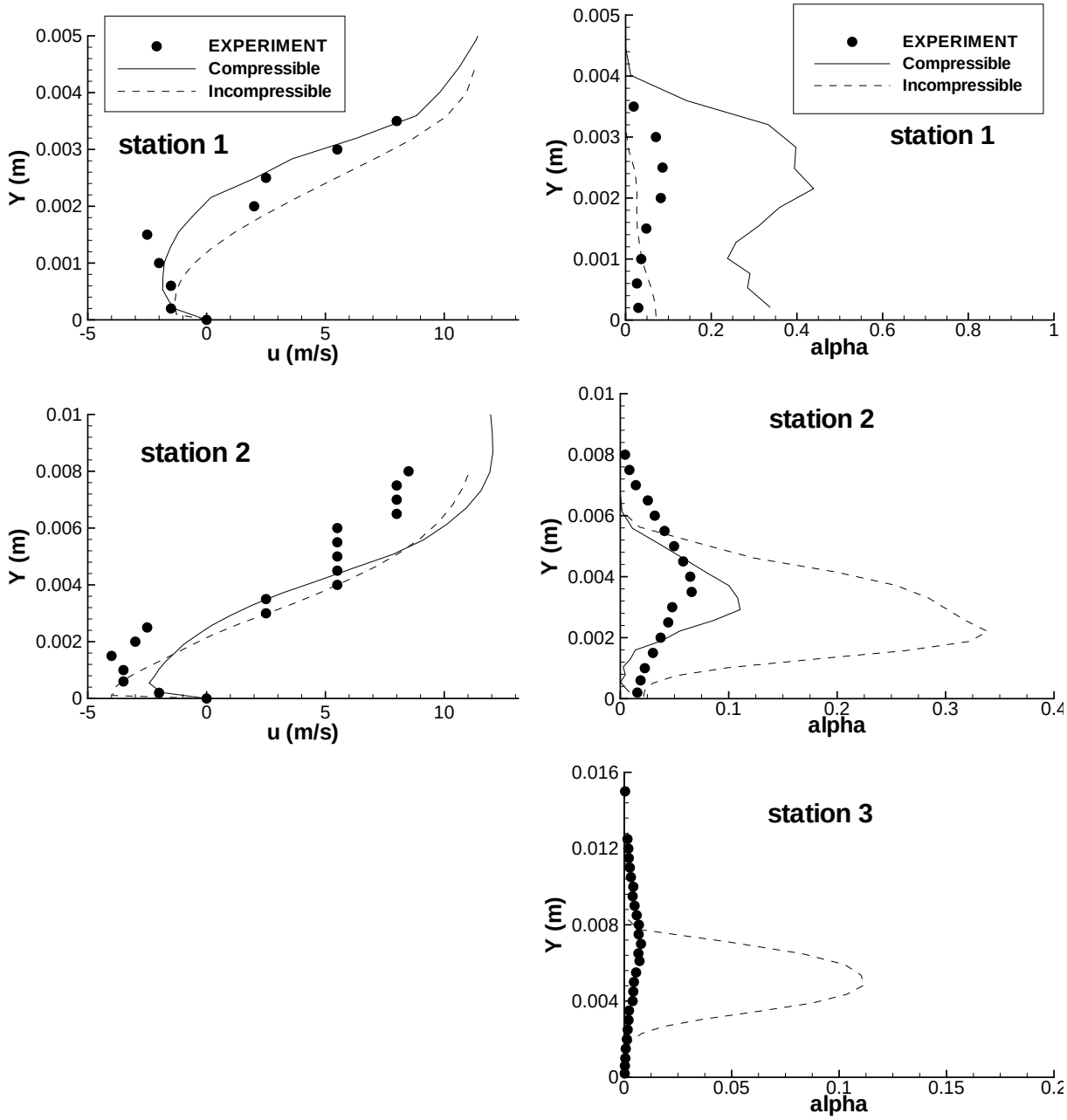

Figure 20. Time-averaged velocity (left) and void ratio (right) profiles, 8° Venturi